

¹ **Global changes in oceanic mesoscale currents over the satellite altimetry record**

³ Josué Martínez-Moreno¹, Andrew McC. Hogg¹, Matthew H. England², Navid C. Constantinou¹,
⁴ Andrew E. Kiss¹ & Adele K. Morrison¹

⁵ ¹*Research School of Earth Sciences and ARC Centre of Excellence for Climate Extremes, Aus-*
⁶ *tralian National University, Canberra, ACT, Australia*

⁷ ²*Climate Change Research Centre and ARC Centre of Excellence for Climate Extremes, Univer-*
⁸ *sity of New South Wales, Sydney, NSW, Australia*

⁹ **Oceanic mesoscale eddies play a profound role in mixing tracers such as heat, carbon, and**
¹⁰ **nutrients, thereby regulating regional and global climate. Yet, it remains unclear how the**
¹¹ **eddy field has varied over the past few decades. Furthermore, climate model predictions**
¹² **generally do not resolve mesoscale eddies, which could limit their accuracy in simulating fu-**
¹³ **ture climate change. Here we show a global statistically significant increase of ocean eddy**
¹⁴ **activity using two independent observational datasets of surface mesoscale eddy variability,**
¹⁵ **one estimates surface currents and the other is derived from sea surface temperature. Maps**
¹⁶ **of mesoscale variability trends show heterogeneous patterns, with eddy-rich regions showing**
¹⁷ **a significant increase of 2% - 5% per decade, while the tropical oceans show a decrease in**
¹⁸ **mesoscale variability. This readjustment of the surface mesoscale ocean circulation has im-**
¹⁹ **portant implications for the exchange of heat and carbon between the ocean and atmosphere.**

²⁰ Changes in the climate system over recent decades have warmed the upper ocean and modi-

21 fied the wind stress, heat and freshwater fluxes that drive ocean circulation^{1,2}. These changes have
22 the capacity to modify the ocean circulation, including the overturning circulation^{3,4}, basin-scale
23 gyres^{5,6} and boundary currents^{7,8}. Changes in climate can also affect mesoscale processes, for
24 example through changes in wind stress forcing over the Southern Ocean⁹. The oceanic mesoscale
25 incorporates motions that occur at spatial scales from approximately 10 to 100 km. These motions
26 include both steady flows (e.g. jets and recirculations) and time-varying flows (e.g. meanders
27 and coherent vortices). Generally, time-varying mesoscale flows are also referred to as eddies.
28 Mesoscale eddies are ubiquitous in the global ocean and feed back onto all scales, from regional
29 processes¹⁰ up to the global meridional overturning circulation³. Moreover, these eddies act to
30 transport and mix tracers such as heat, salt, and nutrients^{11,12}. Thus, understanding the evolution
31 of the mesoscale circulation is crucial to formulating better predictions of our changing oceans.

32 Kinetic energy (KE) quantifies the magnitude of ocean currents^{9,13–15}. Kinetic energy is
33 proportional to the square of the velocity, and is commonly separated into the mean KE (MKE;
34 computed from the time-mean velocity field) and the KE of the time-varying velocity (known as
35 the eddy kinetic energy; EKE). The EKE is dominated by mesoscale variability and is a signif-
36 icant fraction of the total KE^{16,17}. A recent study has inferred a global increase of KE anomaly
37 from ocean reanalyses and Argo floats¹⁵. However, these reanalyses and observations do not have
38 the spatial resolution required to resolve the mesoscale field. Moreover, the ECCO ocean state-
39 estimate shows a slight speed up of the currents, with a weak trend of surface kinetic energy¹⁸.
40 In contrast, satellite observations resolve the mesoscale field at latitudes between 60°S - 60°N,
41 and suggest that EKE in the Southern Ocean and Northeastern Pacific have a robust increasing

42 trend^{9,19–21}. However, the global multi-decadal trends of mesoscale eddy activity from satellite
43 observations are yet to be quantified.

44 Mesoscale flows have a footprint in both sea surface height (SSH) and sea surface temper-
45 ature (SST). EKE can be directly inferred from SSH via geostrophy, and mesoscale eddies act
46 to strain and shear the temperature field, meaning that regions of high EKE are associated with
47 strong mesoscale SST gradients. Therefore, observed SST gradients can be considered a proxy of
48 mesoscale eddies^{22–24}.

49 In this study we examine the evolution of mesoscale eddies using satellite observations of
50 SSH and SST over the satellite altimetry record (1993 - 2020). We use two independent datasets,
51 namely AVISO+ SSH and NOAA optimum interpolated sea surface temperature (OISST v2.1)²⁵,
52 to estimate EKE and SST gradients respectively (see Methods). These fields are then temporally
53 smoothed using a running average of 12 months to eliminate the seasonal cycle. The trends and
54 the significance of each field are computed using a linear regression and a modified Mann–Kendall
55 test²⁶ (see Methods for further details). Mesoscale variability is spatially heterogeneous; thus we
56 explore the trends of mesoscale eddies both globally and regionally.

57 Global mesoscale eddy trends

58 Over the last three decades, ocean thermal expansion and melting of land ice have led to an
59 increase of SSH^{1,27} (Fig. 1a). This SSH increase can be observed in all ocean basins, but there
60 is also regional variability (Fig. 1b). SSH gradients are proportional to the surface geostrophic
61 flow, from which we can compute velocity anomalies and eddy kinetic energy (see Methods). The

62 time-mean EKE highlights eddy-rich regions including boundary currents and their extensions, the
63 Antarctic Circumpolar Current (ACC), and the equatorial band (Fig. 1d). These oceanic eddy-rich
64 regions show statistically significant trends over the satellite altimetry record 1993-2020 (Fig. 1f),
65 which suggest a regional long-term adjustment of the ocean mesoscale eddy field. Moreover, the
66 global surface area-integrated EKE has a positive trend of $\sim 1.2\%$ per decade ($0.09 \pm 0.04 \text{ PJ m}^{-1}$
67 decade $^{-1}$; Fig. 4c; statistically significant at the 95% confidence level). The spatial structure of
68 EKE trends is highly heterogeneous, although its zonal average shows significant net tendencies,
69 with increasing trends observed polewards of 25°S and 40°N (Fig. 1e,f). A strengthening of the
70 EKE field is a direct indication of an increase in mesoscale currents.

71 Sea surface temperature is an independent dataset relative to SSH, but is also influenced by
72 mesoscale eddies and has better temporal and spatial resolution than SSH. SST has increased on
73 multi-decadal timescales due to climate change^{28,29} (Fig. 2a), with a heterogeneous global spa-
74 tial pattern modulated by interdecadal climate variability³⁰ (Fig. 2b). The time-mean SST gradi-
75 ents again highlight eddy-rich regions, such as boundary currents, their extensions, and the ACC
76 (Fig. 2d). These regions with large SST gradients also exhibit some of the largest positive SST
77 gradient trends, while the subtropical gyres and the tropics mostly exhibit a decreasing trend
78 (Fig. 2e,f). The global area-integrated SST gradient magnitude has increased at a rate of $3.9 \pm$
79 $1.33 \times 10^6 \text{ }^\circ\text{C m decade}^{-1}$ (Fig. 4e) or 0.2% per decade (95% confidence level) relative to the
80 global time-mean area-integrated SST gradient magnitude ($1.7 \times 10^9 \text{ }^\circ\text{C m}$). Moreover, SST gra-
81 dients are enhanced by stretching and straining due to mesoscale eddies. Further analysis shows
82 that mesoscale SST gradients (Extended Data Fig. 3; length-scales smaller than 3°; see Methods)

83 dominate the observed trends, increasing at a rate of $5.37 \pm 0.94 \times 10^6 \text{ } ^\circ\text{C m decade}^{-1}$ (0.4% per
84 decade; statistically significant at the 95% confidence level). This analysis confirms that the ob-
85 served SST gradient trends are a consequence of the mesoscale eddy field stirring the temperature
86 field.

87 Eddy kinetic energy and mesoscale SST gradients show analogous spatial and temporal re-
88 sponses in the boundary currents and their extensions, the ACC and the tropics. Note that eddy-rich
89 regions such as the Kuroshio Current, the Agulhas retroflection, the Gulf Stream, and the East Aus-
90 tralian Current show large changes in mesoscale SST gradients co-located with some of the largest
91 EKE changes (Fig. 3). Even though these fields do not match perfectly, we quantified the areas of
92 same-sign trend for each of these four regions (Extended Data Fig. 4). We find that the increasing
93 and decreasing trends of SST and EKE match to a good extent for the Kuroshio Current, the Agul-
94 has retroflection, and the East Australian Current (61% - 65% of same-sign area agreement). The
95 spatial patterns of these independent satellite products further suggest an intrinsic response of the
96 mesoscale eddy field to a changing and variable climate.

97 **Spatial patterns of ocean mesoscale trends**

98 Eddy kinetic energy and mesoscale SST gradient trends both indicate a net strengthening of
99 the global mesoscale activity. However, both datasets reveal heterogeneous patterns of increas-
100 ing and decreasing trends. Thus, to further understand the spatial variability, we first focus our
101 analysis on individual area-integrated regions: namely, the Southern Ocean (by which we mean
102 south of 35°S), and the Pacific, Indian, and Atlantic Oceans north of 35°S (Fig. 4d). This analysis

103 reveals that the Southern Ocean and the Pacific Ocean are, to a large extent, responsible for the
104 global area-integrated trends and variations of EKE and mesoscale SST gradients; the trends in the
105 Indian and Atlantic Oceans are in contrast much smaller (Fig. 4a,b). The Southern Ocean shows
106 a statistically significant increase for both the EKE and SST gradient, where the observed changes
107 have been attributed to the strengthening of the wind stress since the early 1990s⁹. The Pacific
108 Ocean SST gradient decreases significantly, with the EKE signal also decreasing; albeit below the
109 95% significance level (Fig. 4c,e). The large uncertainty in the Pacific EKE trend (orange error
110 bars in Fig. 4c) is a consequence of the pulses in the time series during 1997 and 2015, both being
111 El Niño onset years. These large anomalous interannual signals dominate the uncertainty of the
112 global EKE trend.

113 El Niño events are associated with a strengthening of the North Equatorial Countercurrent
114 and the northern branch of the South Equatorial Current; particularly during extreme eastern Pa-
115 cific El Niños, such as those which occurred during 1997-1998 and 2015-2016³¹ (gray bars in
116 Fig. 4a,b). During such El Niño events, the equatorial currents generate significant transient circu-
117 lation anomalies that extend over the equatorial band (9°N - 9°S). After a scale decomposition of
118 the velocities, we observe that these EKE pulses correspond to features located within the equato-
119 rial band and have scales larger than the typical mesoscale eddy size¹¹ (approximately 10 to 100
120 km; see Methods; Extended Data Fig. 5a,c). Thus, equatorial currents during El Niño events mod-
121 ulate the equatorial EKE response and the strong interannual variability conceals EKE trends over
122 the equatorial region.

123 To further investigate the effect of El Niño events on the mesoscale, we remove the equato-
124 rial regions (9°S – 9°N) and repeat the global trend analysis for EKE and SST gradients. The global
125 area-integrated extra-tropical EKE and SST gradient trends increase, while the corresponding rel-
126 ative uncertainty decreases; namely, EKE trends are $1.8\% \pm 0.25\%$ per decade and mesoscale SST
127 gradients trends are $1.6\% \pm 0.09\%$ per decade (see striped bars in Fig. 4c,e); both significant at the
128 95% confidence level. It is thus clear that mesoscale activity in the Pacific, and particularly in the
129 equatorial region, is strongly influenced by interannual variability.

130 **Eddy-rich regions become richer**

131 The observed changes in EKE and SST of whole ocean basins integrate over large heteroge-
132 neous regions with opposing trends. For example, the Pacific Ocean aggregates the strengthening
133 of the equatorial currents in the equatorial Pacific Ocean during El Niño events, boundary currents,
134 and the broader-scale oceanic gyres. These dynamical regions are not unique to the Pacific Ocean;
135 the Atlantic and Indian basins also span diverse dynamical regions. Therefore, we further decom-
136 pose the ocean into dynamical regions (Fig. 5d): namely, (1) the Antarctic Circumpolar Current
137 (ACC) and surrounds, (2) the boundary currents and their extensions, (3) the equatorial regions,
138 and (4) the subtropical ocean gyres (see Methods for dynamical region definitions). The remaining
139 regions are aggregated into a fifth group. We then investigate the variability and trends within each
140 of these dynamical sub-regions.

141 Globally, there is a significant increase of EKE and SST gradients, however, each dynami-
142 cal region shows a different response (Fig. 5). For example, the ACC region shows a significant

increase in both EKE and SST gradients at rates of 5.1% and 3% per decade (Fig. 5c,e), consistent with an increase in eddy activity with strengthening wind stress, as demonstrated in previous studies^{9,13,20}. Boundary currents and their extensions collectively show a similar net response, in which EKE and SST gradients both increase at rates of 2.5% and 8.1% per decade respectively. Individually, SST gradients increase in all boundary currents, however EKE in the Agulhas retroflection, the East Australian Current, the Leeuwin Current, and the Malvinas Current have significantly increased, but the Gulf Stream and the Kuroshio Current do not show a significant net strengthening^{32,33}(Extended Data Fig. 6); instead, regions of increase and decrease tend to cancel each other out in an area-integral. This cancellation is particularly evident for the Kuroshio Current (Fig. 1f and Extended Data Fig. 6b). The response seen in the Gulf Stream and Kuroshio Current is consistent a poleward shift in these currents^{7,34,35} and a readjustment to climate modes³⁶. Note that a poleward shift cannot be captured by our static climatological definition of the boundary currents regions (see Methods). Thus, a shift of the boundary currents will result in an increase of EKE and SST gradients outside our dynamical definitions (i.e. in regions poleward of the boundary currents and ocean gyres; white regions in Fig. 5d). The observed strengthening of these remaining regions is comparable to that of the ACC, and suggests a poleward shift of the boundary currents, particularly in the Northern Hemisphere.

The equatorial and subtropical gyre regions exhibit statistically significant negative SST gradient trends, and statistically non-significant negative EKE trends (Fig. 5), suggesting a reduction of the mesoscale eddy variability of the equatorial region and the interior of the subtropical gyres (Fig. 2). The equatorial region is dominated by interannual variability, where large changes corre-

¹⁶⁴ sponding to El Niño events occur in both the EKE and SST gradient time series. The significant
¹⁶⁵ decrease of SST gradients in the subtropical gyres could result from the displacement of the ex-
¹⁶⁶ tratropical atmospheric circulation^{37,38} and the expansion of the tropics³⁹. The decreasing SST
¹⁶⁷ gradient trends in the tropics could be due to a homogenization of the tropical surface SST gra-
¹⁶⁸ dients. In the future, the SST gradients induced by mesoscale stirring are expected to reduce as
¹⁶⁹ the surface ocean becomes more thermally homogeneous. However, a longer record is required to
¹⁷⁰ separate the mesoscale response from interannual-decadal climate variability.

¹⁷¹ We have analyzed the available satellite altimetry record of SSH and SST to reveal a signifi-
¹⁷² cant global intensification of the mesoscale eddy field over the satellite record. While the observed
¹⁷³ global surface percentage increases per decade may seem small ($\sim 0.5\%$ per decade), like ocean
¹⁷⁴ heat content and sea-level trends, even small fractions of a percentage change correspond to a large
¹⁷⁵ energy perturbation of the earth system. For example, if we assume that the mesoscale flow ex-
¹⁷⁶ tends vertically to around 500 m depth (a reasonable assumption given the vertical structure of the
¹⁷⁷ gravest mode⁴⁰), then the observed EKE trends integrated over 500 m imply a significant increase
¹⁷⁸ of 0.78% in the global volume-integrated mesoscale energy budget ($13 \times 10^{18} \text{ J}$ ⁴¹) over the satel-
¹⁷⁹ lite altimetry record after removing the El Niño signal (Extended Data Fig. 5b). This percentage is
¹⁸⁰ equivalent to $1.03 \times 10^{17} \text{ J}$, the same order of magnitude as the global internal tide energy budget
¹⁸¹ ($1 \times 10^{17} \text{ J}$ ⁴¹). Eddy kinetic energy in eddy-rich regions, such as boundary current extensions and
¹⁸² the ACC, exhibit even larger significant strengthening of 2% and 5%, respectively (see Fig. 5).
¹⁸³ Increased mesoscale activity observed in both SST and mesoscale SST gradients is most apparent
¹⁸⁴ in regions where eddies are already strong. These eddy-rich regions are critical for carbon and heat

185 uptake by the ocean^{42,43}, and they are known to be sensitive to climate modes that are readjusting
186 in a changing climate; for example, the strengthening of the westerly winds⁹ linked to recent in-
187 creasing trends in the Southern Annular Mode^{44,45}. With ongoing future projected changes in the
188 westerly wind belt, it is expected that mesoscale activity in the southern hemisphere boundary cur-
189 rents and the ACC will continue to increase over the coming decades. Current generation models
190 used for climate projections (CMIP6) do not generally resolve mesoscale eddies⁴⁶; thus, important
191 climatic adjustments driven by changes in the eddy field are likely to be missing from these climate
192 projections.

193 The mesoscale evolution described here cannot be captured by coarse-resolution reanalysis
194 products and sparse Argo float observations, as previously used in other studies¹⁵. Here we have
195 used eddy-permitting satellite observations to reveal a potential decrease in EKE over the tropics,
196 while reanalysis products suggest the tropics is where KE anomalies have increased the most¹⁵.
197 The KE anomaly differs from EKE because it contains the time-mean flow in addition to the time-
198 varying components. The source of differences between Hu *et al.*, (2020)¹⁵ and our results can be
199 assessed by an analysis of the ocean KE anomaly using satellite observations. The KE anomaly
200 trends are almost identical to the EKE trends presented above (compare Fig. 1 and Extended Data
201 Fig. 7), yet strikingly different from those obtained by Hu *et al.*, (2020) (their Fig 2a). This sug-
202 gests that the difference between our results and those of Hu *et al.*, (2020) arises from the inability
203 of reanalyses and the Argo dataset to resolve the mesoscale, due to coarse-resolution and sparse
204 sampling, rather than from the definition of the KE anomaly. An alternative explanation of the
205 differences between our study and Hu *et al.*, (2020) could arise from the KE anomaly trends in Hu

206 *et al.*, (2020) being depth-integrated (0-2000 m), while our EKE calculations are derived solely
207 from surface diagnostics. In addition, as we have demonstrated, the tropics are strongly influenced
208 by interannual variability (e.g. El Niño), and yet the KE time-series from coarse reanalysis data
209 does not detect the two extreme El Niño events observed in the satellite record. Thus, data res-
210 olution and/or subsurface ocean dynamics are the likely causes of the discrepancy between our
211 eddy-permitting analysis and the results from prior work using reanalysis products¹⁵.

212 There are several possible causes of the observed trends in mesoscale activity including (1)
213 changes in winds (wind curl, wind stress), (2) changes in stratification, and (3) changes in large-
214 scale horizontal temperature gradients. These forcing agents can impact the eddy activity via
215 a combination of processes, e.g., non-local intensification of winds, outcropping and tilting of
216 isopycnals, and strengthening of baroclinic instability. Atmospheric reanalyses show distinct and
217 inconsistent wind stress trend patterns, while records of *in situ* measurements of isopycnal tilt and
218 baroclinic growth rate are too short and too sparse to provide evidence of a dynamical mechanism
219 driving the observed increase in eddy activity. Thus, longer observational records with higher tem-
220 poral and spatial frequency are required to better understand the increase in EKE observed from
221 satellites. In addition, as discussed above, trends computed from coarse-resolution ocean reanaly-
222 sis products¹⁵ with parameterized mesoscale eddies differ significantly from the mesoscale trends
223 we detect from eddy-resolving satellite altimetry. Hence, an in-depth analysis of the dynamics
224 leading to the observed mesoscale eddy evolution should be explored in more detail using truly
225 eddy-resolving global ocean models or eddy-resolving reanalysis products.

226 Our study has documented a major global-scale reorganization of the ocean's mesoscale
227 kinetic energy observed over the past three decades. These observed adjustments in the mesoscale
228 field have the potential to affect ocean circulation at regional and global scales, and to modify
229 the transport and redistribution of tracers, such as heat, carbon, and nutrients. Our findings thus
230 have major implications for ocean readjustment to a changing climate, as the enhancement of the
231 mesoscale ocean currents may feed back on the sequestration of anthropogenic heat and carbon
232 into the ocean.

233 1. Pörtner, H. *et al.* IPCC, 2019: IPCC special report on the ocean and cryosphere in a changing
234 climate. *IPCC 2019* 42 (2019).

235 2. Intergovernmental Panel on Climate Change. Working Group 1, S. *et al.* *Climate Change 2007*
236 - *The Physical Science Basis: Working Group I Contribution to the Fourth Assessment Report*
237 *of the IPCC.* Assessment report (Intergovernmental Panel on Climate Change).: Working
238 Group (Cambridge University Press, 2007).

239 3. Marshall, J., Scott, J. R., Romanou, A., Kelley, M. & Leboissetier, A. The dependence of the
240 ocean's MOC on mesoscale eddy diffusivities: A model study. *Ocean Modelling* **111**, 1–8
241 (2017).

242 4. Toggweiler, J. R. & Russell, J. Ocean circulation in a warming climate. *Nature* **451**, 286–8
243 (2008).

244 5. Yang, H. *et al.* Poleward Shift of the Major Ocean Gyres Detected in a Warming Climate.
245 *Geophysical Research Letters* **47** (2020).

- 246 6. Sutton, R. T. & Hodson, D. L. R. Climate Response to Basin-Scale Warming and Cooling of
247 the North Atlantic Ocean. *Journal of Climate* **20**, 891–907 (2007).
- 248 7. Wu, L. *et al.* Enhanced warming over the global subtropical western boundary currents. *Nature
249 Climate Change* **2**, 161–166 (2012).
- 250 8. Kwon, Y.-O. *et al.* Role of the Gulf Stream and Kuroshio–Oyashio Systems in Large-Scale
251 Atmosphere–Ocean Interaction: A Review. *Journal of Climate* **23**, 3249–3281 (2010).
- 252 9. Hogg, A. M. *et al.* Recent trends in the Southern Ocean eddy field. *Journal of Geophysical
253 Research: Oceans* **120**, 257–267 (2015).
- 254 10. Radko, T. & Marshall, J. Eddy-Induced Diapycnal Fluxes and Their Role in the Maintenance
255 of the Thermocline. *Journal of Physical Oceanography* **34**, 372–383 (2004).
- 256 11. Chelton, D. B., Gaube, P., Schlax, M. G., Early, J. J. & Samelson, R. M. The influence of
257 nonlinear mesoscale eddies on near-surface oceanic chlorophyll. *Science* **334**, 328–32 (2011).
- 258 12. Early, J. J., Samelson, R. M. & Chelton, D. B. The Evolution and Propagation of Quasi-
259 geostrophic Ocean Eddies. *Journal of Physical Oceanography* **41**, 1535–1555 (2011).
- 260 13. Meredith, M. P., Garabato, A. C., Hogg, A. M. & Farneti, R. Sensitivity of the Overturning
261 Circulation in the Southern Ocean to Decadal Changes in Wind Forcing. *Journal of Climate*
262 **25**, 99–110 (2012).
- 263 14. Busecke, J. J. M. & Abernathey, R. P. Ocean mesoscale mixing linked to climate variability.
264 *Science Advances* **5**, eaav5014 (2019).

- 265 15. Hu, S. *et al.* Deep-reaching acceleration of global mean ocean circulation over the past two
266 decades. *Science Advances* **6**, eaax7727 (2020).
- 267 16. Wyrtki, K., Magaard, L. & Hager, J. Eddy energy in the oceans. *Journal of Geophysical*
268 *Research* **81**, 2641–2646 (1976).
- 269 17. Chelton, D. B., Schlax, M. G., Samelson, R. M. & de Szoeke, R. A. Global observations of
270 large oceanic eddies. *Geophysical Research Letters* **34**, L15606 (2007).
- 271 18. Wunsch, C. Is The Ocean Speeding Up? Ocean Surface Energy Trends. *Journal of Physical*
272 *Oceanography* **50**, 1–45 (2020).
- 273 19. Patara, L., Böning, C. W. & Biastoch, A. Variability and trends in Southern Ocean eddy activ-
274 ity in 1/12° ocean model simulations. *Geophysical Research Letters* **43**, 4517–4523 (2016).
- 275 20. Martínez-Moreno, J., Hogg, A. M., Kiss, A. E., Constantinou, N. C. & Morrison, A. K. Kinetic
276 energy of eddy-like features from sea surface altimetry. *Journal of Advances in Modeling*
277 *Earth Systems* **11**, 3090–3105 (2019).
- 278 21. Ding, M., Lin, P., Liu, H. & Chai, F. Increased Eddy Activity in the Northeastern Pacific
279 during 1993–2011. *Journal of Climate* **31**, 387–399 (2017).
- 280 22. Yuan, Y. & Castelao, R. M. Eddy-induced sea surface temperature gradients in Eastern Bound-
281 ary Current Systems. *Journal of Geophysical Research: Oceans* **122**, 4791–4801 (2017).
- 282 23. Castellani, M. Identification of eddies from sea surface temperature maps with neural net-
283 works. *International Journal of Remote Sensing* **27**, 1601–1618 (2006).

- 284 24. Holladay, C. G. & O'Brien, J. J. Mesoscale Variability of Sea Surface Temperatures. *Journal*
285 *of Physical Oceanography* **5**, 761–772 (1975).
- 286 25. Banzon, V., Smith, T. M., Steele, M., Huang, B. & Zhang, H.-M. Improved Estimation of
287 Proxy Sea Surface Temperature in the Arctic. *Journal of Atmospheric and Oceanic Technology*
288 **37**, 341–349 (2020).
- 289 26. Yue, S. & Wang, C. The Mann-Kendall Test Modified by Effective Sample Size to Detect
290 Trend in Serially Correlated Hydrological Series. *Water Resources Management* **18**, 201–218
291 (2004).
- 292 27. Polito, P. S. & Sato, O. T. Global Interannual Trends and Amplitude Modulations of the
293 Sea Surface Height Anomaly from the TOPEX/ Jason-1 Altimeters. *Journal of Climate* **21**,
294 2824–2834 (2008).
- 295 28. Cane, M. A. *et al.* Twentieth-Century Sea Surface Temperature Trends. *Science* **275**, 957–960
296 (1997).
- 297 29. Ruela, R., Sousa, M. C., deCastro, M. & Dias, J. M. Global and regional evolution of sea
298 surface temperature under climate change. *Global and Planetary Change* **190**, 103190 (2020).
- 299 30. Cane, M. A. *et al.* Twentieth-Century Sea Surface Temperature Trends. *Science* **275**, 957–960
300 (1997).
- 301 31. Wang, L.-C. & Wu, C.-R. Contrasting the Flow Patterns in the Equatorial Pacific Between
302 Two Types of El Niño. *Atmosphere-Ocean* **51**, 60–74 (2013).

- 303 32. Ezer, T., Atkinson, L. P., Corlett, W. B. & Blanco, J. L. Gulf Stream's induced sea level rise
304 and variability along the U.S. mid-Atlantic coast: Gulf Stream induces coastal sea level rise.
305 *Journal of Geophysical Research: Oceans* **118**, 685–697 (2013).
- 306 33. Uchida, H. & Imawaki, S. Estimation of the sea level trend south of Japan by combining
307 satellite altimeter data with in situ hydrographic data. *Journal of Geophysical Research* **113**
308 (2008).
- 309 34. Wu, B., Lin, X. & Yu, L. Poleward Shift of the Kuroshio Extension Front and its Impact
310 on the North Pacific Subtropical Mode Water in the Recent Decades. *Journal of Physical*
311 *Oceanography* (2020).
- 312 35. Yang, H. *et al.* Intensification and poleward shift of subtropical western boundary currents in
313 a warming climate. *Journal of Geophysical Research: Oceans* **121**, 4928–4945 (2016).
- 314 36. Piecuch, C. G. Likely weakening of the Florida Current during the past century revealed by
315 sea-level observations. *Nature Communications* **11**, 3973 (2020).
- 316 37. Saenko, O. A., Fyfe, J. C. & England, M. H. On the response of the oceanic wind-driven
317 circulation to atmospheric CO₂ increase. *Climate Dynamics* **25**, 415–426 (2005).
- 318 38. Sen Gupta, A. *et al.* Projected Changes to the Southern Hemisphere Ocean and Sea Ice in the
319 IPCC AR4 Climate Models. *Journal of Climate* **22**, 3047–3078 (2009).
- 320 39. Seidel, D. J., Fu, Q., Randel, W. J. & Reichler, T. J. Widening of the tropical belt in a changing
321 climate. *Nature Geoscience* **1**, 21–24 (2007).

- 322 40. Sanchez de La Lama, M., LaCasce, J. H. & Fuhr, H. K. The vertical structure of ocean eddies.
- 323 *Dynamics and Statistics of the Climate System* **1**, dzw001 (2016).
- 324 41. Wunsch, C. & Ferrari, R. Vertical mixing, energy and the general circulation of oceans. *Annual*
- 325 *Review of Fluid Mechanics* **36**, 281–314 (2004).
- 326 42. Foppert, A. *et al.* Eddy heat flux across the Antarctic Circumpolar Current estimated from sea
- 327 surface height standard deviation. *Journal of Geophysical Research: Oceans* **122**, 6947–6964
- 328 (2017).
- 329 43. Gnanadesikan, A., Pradal, M.-A. & Abernathey, R. Isopycnal mixing by mesoscale eddies
- 330 significantly impacts oceanic anthropogenic carbon uptake. *Geophysical Research Letters* **42**,
- 331 4249–4255 (2015).
- 332 44. Abram, N. J. *et al.* Evolution of the Southern Annular Mode during the past millennium.
- 333 *Nature Climate Change* **4**, 564–569 (2014).
- 334 45. Gillett, N. P. & Fyfe, J. C. Annular mode changes in the CMIP5 simulations. *Geophysical*
- 335 *Research Letters* **40**, 1189–1193 (2013).
- 336 46. Haarsma, R. J. *et al.* High Resolution Model Intercomparison Project (HighResMIP v1.0) for
- 337 CMIP6. *Geoscientific Model Development* **9**, 4185–4208 (2016).
- 338 47. Wolter, K. & Timlin, M. S. Measuring the strength of ENSO events: How does 1997/98 rank?
- 339 *Weather* **53**, 315–324 (1998).

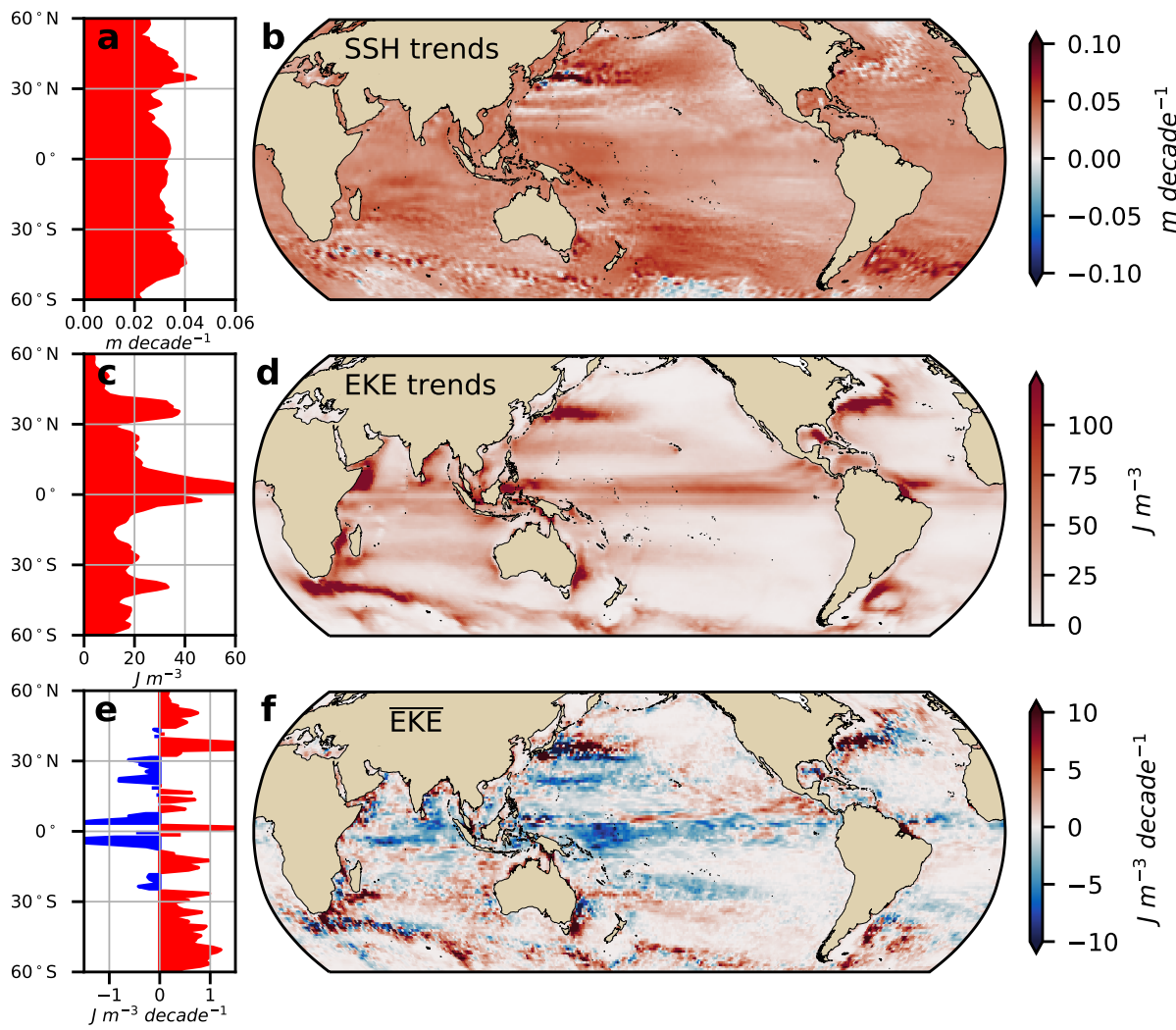
340 48. Lagerloef, G. S. E., Mitchum, G. T., Lukas, R. B. & Niiler, P. P. Tropical Pacific near-surface
341 currents estimated from altimeter, wind, and drifter data. *Journal of Geophysical Research: Oceans* **104**, 23313–23326 (1999).

343 **Acknowledgments**

344 We thank Ryan Holmes for clarifying the equatorial response of El Niño events during 1997-
345 1998 and 2015-2016. We thank the reviewers for their insightful comments and suggestions. The
346 satellite altimetry products were produced by Ssalto/Duacs and distributed by AVISO+, with sup-
347 port from CNES (<https://www.aviso.altimetry.fr/en/data/products/sea-surface-heights-global/gridded-sea-level-heights-and-derived-variables.html>). J. M.-
348 M. was supported by the Consejo Nacional de Ciencia y Tecnología (CONACYT), Mexico fund-
349 ing. M.H.E. was supported by the Centre for Southern Hemisphere Oceans Research (CSHOR),
350 a joint research centre between QNLM, CSIRO, UNSW and UTAS. A. K. M. was supported by
351 the Australian Research Council DECRA Fellowship DE170100184. Analyses were undertaken
352 on the National Computational Infrastructure in Canberra, Australia, which is supported by the
353 Australian Commonwealth Government.

355 **Author contributions**

356 J.M.M, A.McC.H. and M.H.E. conceived the study. J.M.M. conducted the analyses. All
357 authors contributed to interpretation, writing and revision of the manuscript.



358

359

360

361

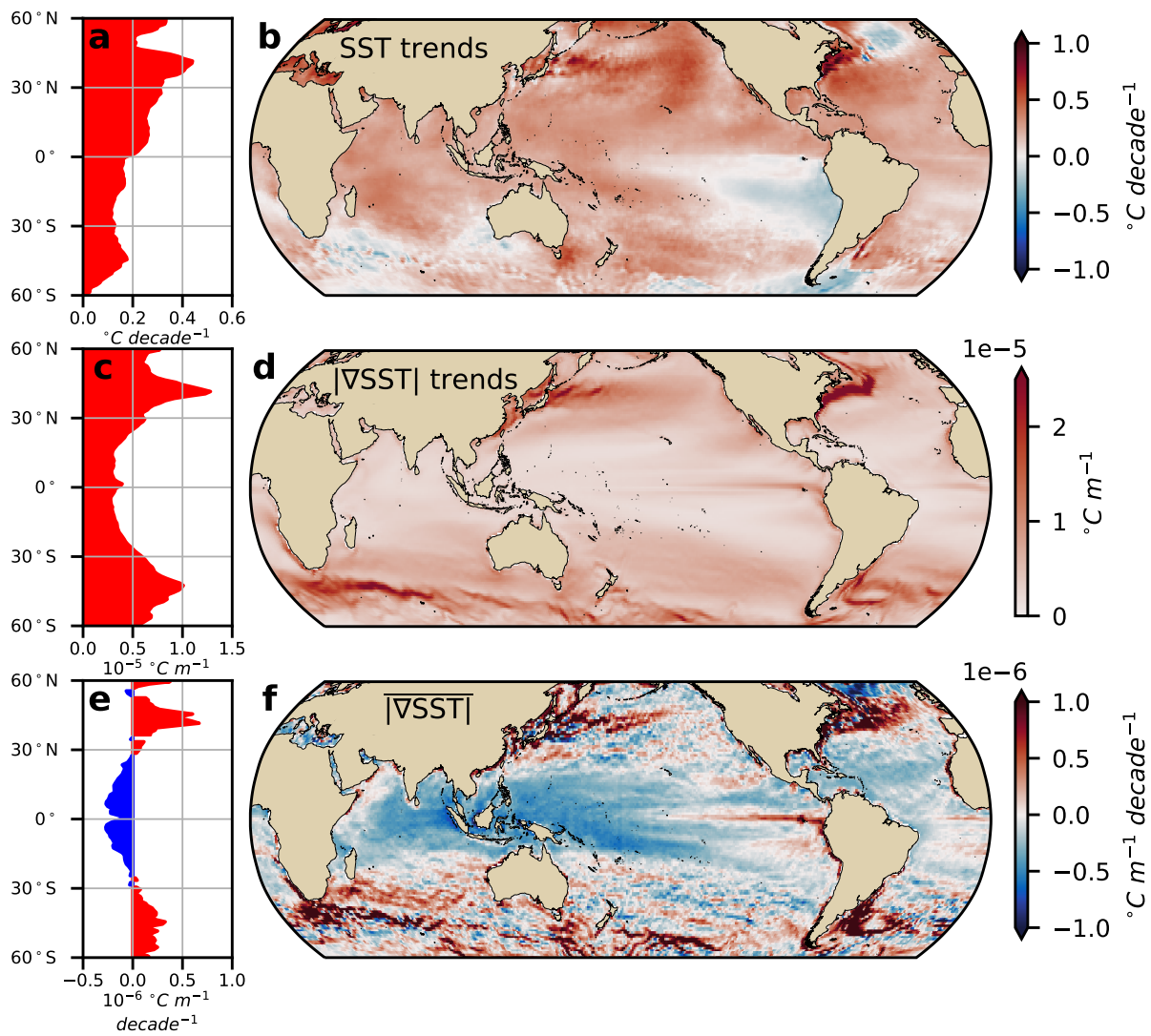
362

363

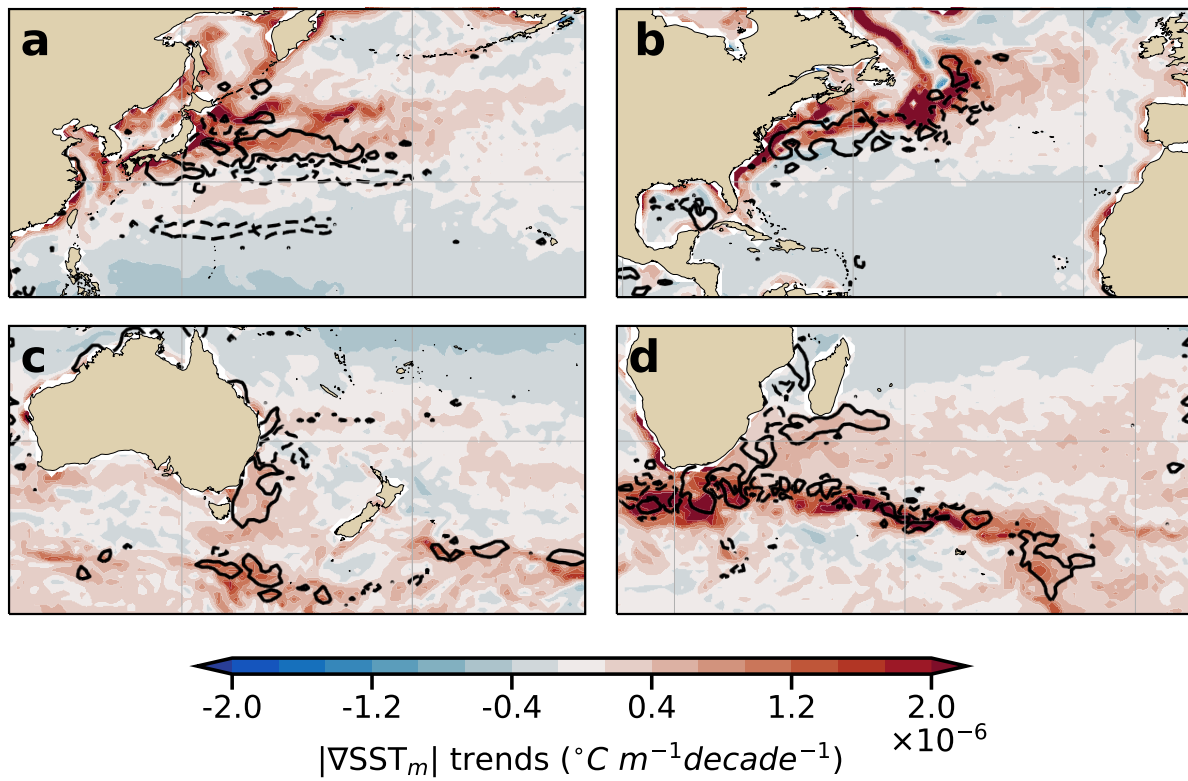
364

365

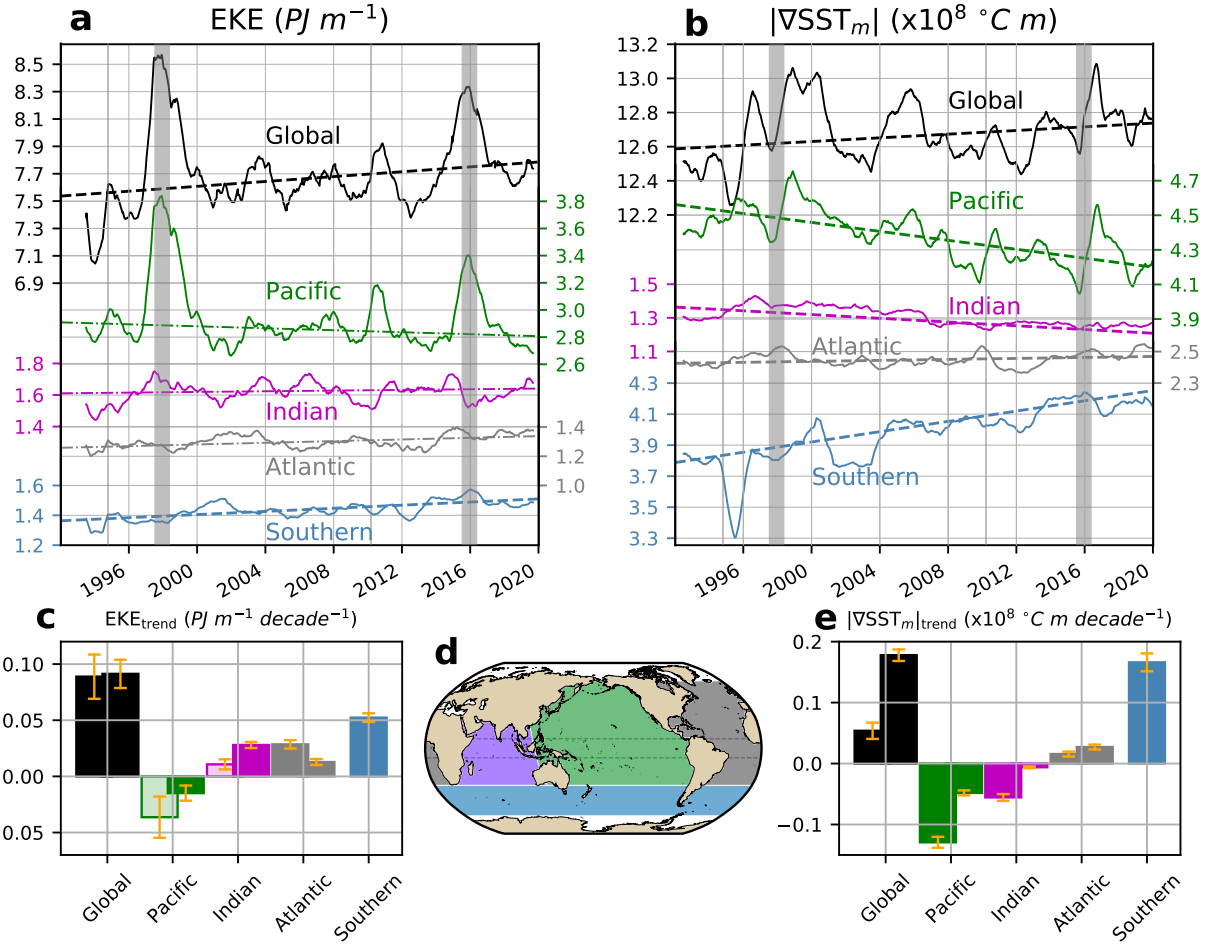
Figure 1 Sea surface height (SSH) trend, mean surface eddy kinetic energy (EKE) and surface eddy kinetic energy trend between 1993-2020 (a) Zonally averaged SSH trend; (b) map of SSH trend (92.1% of area is statistically significant above the 95% confidence level; for spatial distribution refer to Extended Data Fig. 1a); (c) zonally averaged mean EKE; (d) map of mean EKE; (e) zonally averaged EKE trend; (f) map of EKE trend (55.4% of area is statistically significant above the 95% confidence level; see Extended Data Fig. 1b).



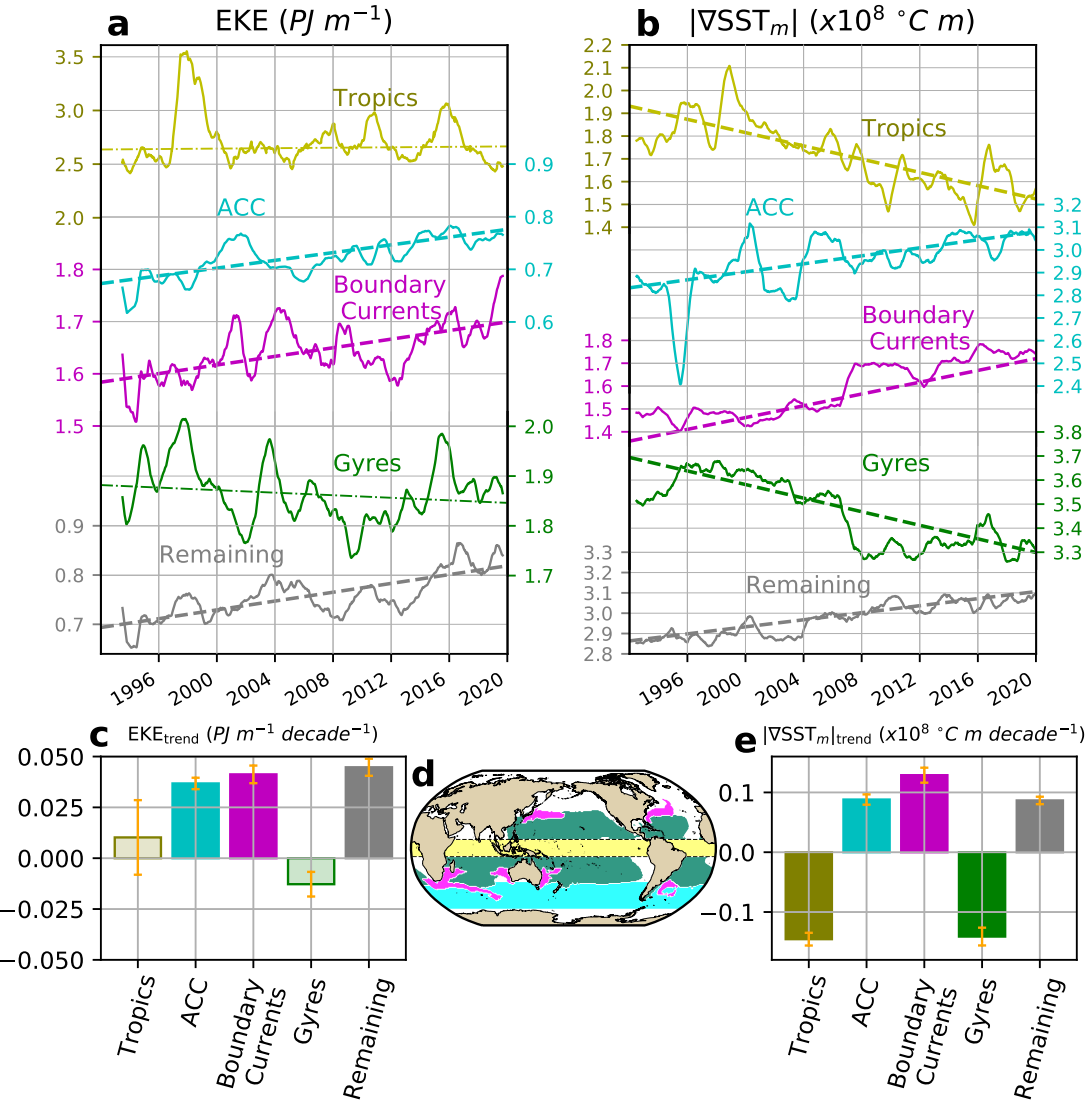
366
367 **Figure 2 Sea surface temperature (SST) trends, mean SST gradient magnitude, and**
368 **SST gradient magnitude trends between 1993-2020.** (a) Zonally averaged SST trend;
369 (b) map of SST trend (76.7% of area is statistically significant above the 95% confidence
370 level; for the spatial distribution refer to Extended Data Fig. 1c); (c) zonally averaged
371 time-mean of SST gradient magnitude; (d) map of time-mean of SST gradient magnitude;
372 (e) zonally averaged SST gradient magnitude trend; (f) map of SST gradient magnitude
373 trends (81.6% of area is statistically significant above the 95% confidence level; see Ex-
374 tended Data Fig. 1d). Note that the spatial pattern of SST gradient maps is independent
375 of the temporal extent of the SST gradient record used to compute SST gradient trends
376 (Extended Data Fig. 2).



377
 378 **Figure 3 Regional maps of mesoscale SST gradient magnitude trends and surface**
 379 **EKE trends.** (a) Kuroshio Current; (b) Gulf Stream; (c) East Australian Current; (d) Ag-
 380 ulhas retroreflection. In all panels, mesoscale SST gradient magnitude trends are shown
 381 by the background color, solid contours show positive EKE trends and dashed contours
 382 show negative EKE trends (contours of $\pm 5 \text{ J } m^{-3} \text{ decade}^{-1}$).



383
384 **Figure 4 Time-series and linear trends of area integrated surface EKE and mesoscale**
385 **SST gradient magnitudes over various ocean basins.** Global (solid black), Southern
386 (blue), Indian (magenta), Pacific (green), and Atlantic Oceans (gray) and each region
387 separately without the equatorial region (striped bars). (a) Surface EKE time series. (b)
388 mesoscale SST gradient magnitude time series. In panels (a) and (b), solid curves de-
389 note 12-month running averages for each basin, dashed lines correspond to statistically
390 significant time-series trends, dashed-dotted lines show statistically insignificant time-
391 series trends, and vertical gray bars indicate El Niño events (above the 90th percentile
392 of MEI.v2⁴⁷). Note that the y axis is discontinuous in panels (a) and (b). (c) Linear EKE
393 trends for each basin. (d) Ocean basins; equatorial region (9°S–9°N) is marked by the
394 dashed lines. (e) Linear mesoscale SST gradient trends. In panels (c) and (e), stan-
395 dard errors are shown with orange bars and statistically significant trends (above the 95%
396 confidence level) are solid bars while non-significant trends are translucent.



397
398 **Figure 5 Time-series and linear trends of integrated surface EKE and mesoscale**
399 **SST gradient magnitudes over dynamical regions.** Global ocean (black), Tropics (yellow),
400 Antarctic Circumpolar Current (cyan), boundary currents and their extensions (magenta),
401 subtropical ocean gyres (green) and the rest (gray). (a) Surface EKE time-series.
402 (b) mesoscale SST gradient magnitude time-series. In panels (a) and (b), solid color
403 curves are 12-month running for each region, dashed lines correspond to statistically sig-
404 nificant time-series trends, and dashed-dotted lines show insignificant time-series trends.
405 (c) Linear EKE trends for each dynamical region. (d) Definition of ocean regions. (e) Lin-
406 ear mesoscale SST gradient trends. Note that in panel (a) the top curve that corresponds
407 to the Tropics has a different scale than the rest. In panels (c) and (e), standard errors
408 are shown with orange bars and statistically significant trends (above the 95% confidence
409 level) are solid bars while non-significant trends are translucent.

410 **Methods**

411 **Observational products**

412 The data used in this study includes sea surface height, geostrophic velocities, and sea sur-
413 face temperature. The Archiving, Validation and Interpretation of Satellite Oceanographic data
414 (AVISO+) gridded multi-mission sea surface height and geostrophic velocities have a horizontal
415 resolution of $1/4^\circ$ (although the effective resolution may be coarser in some regions ¹¹). Currents
416 within the equatorial region ($5^\circ S$ - $5^\circ N$) are estimated using an equatorial β -plane approximation
417 of the geostrophic equations⁴⁸. National Oceanic and Atmospheric Administration - Optimum In-
418 terpolation Sea Surface Temperature (NOAA-OISST) has a horizontal resolution of $1/4^\circ$ ²⁵. This
419 dataset is constructed by combining observations from different products (e.g. satellites, ships,
420 buoys, and Argo floats).

421 These datasets have a quasi-global coverage ($65^\circ S$ - $65^\circ N$) and span 27 years, from January
422 1993 to March 2020. The SST product is available for a longer duration, but we only analyze the
423 period of overlap with the AVISO+ record (see Extended Data Fig. 2). Anomalies were computed
424 with respect to the record's climatology. We have verified that using a different period for defining
425 the climatology does not change the observed trends in the anomaly fields. We have also veri-
426 fied through wavelet analysis of the time-series at individual points that there is no evidence that
427 steps in the record occurred due to improved technology in satellite missions and oceanographic
428 observations.

429 **Kinetic energy decomposition**

430 Kinetic energy (KE) density is decomposed into the energy density contained by the steady
 431 flow (time-mean) and that contained by the transient flow (time-varying). In other words, the
 432 surface geostrophic velocity components are split using a Reynolds decomposition into their time-
 433 mean (\bar{u} , \bar{v}) and time-varying components ($u' = u - \bar{u}$, $v' = v - \bar{v}$), with bars denoting time-
 434 averages over the whole record. The terms u' and v' are the anomalies of the surface geostrophic
 435 velocities provided by AVISO+, which are proportional to the AVISO+ SSH gradients (via the
 436 geostrophic approximation and equatorial beta-plane approximation). The KE is, therefore, de-
 437 composed as:

$$438 \underbrace{\frac{1}{2}\rho_0(u^2 + v^2)}_{\text{KE}} = \underbrace{\frac{1}{2}\rho_0(u'^2 + v'^2)}_{\text{EKE}} + \underbrace{\frac{1}{2}\rho_0(\bar{u}^2 + \bar{v}^2)}_{\text{MKE}} + \underbrace{\rho_0(\bar{u}u' + \bar{v}v')}_{\text{Cross terms}}, \quad (1)$$

439 where we approximate the density of the seawater by the constant $\rho_0 = 1025 \text{ kg m}^{-3}$. The
 440 energy contained in the time-varying component of the flow is known as the eddy kinetic energy
 441 (EKE), while the mean kinetic energy (MKE) is the energy of the time-mean flow.

442 Maps of EKE in this study correspond to the the time-mean EKE, defined as

$$443 \overline{\text{EKE}}(x, y) = \overline{\frac{1}{2}\rho_0(u'^2 + v'^2)}, \quad (2)$$

444 where the units of $\overline{\text{EKE}}(x, y)$ are Jm^{-3} . Time-series correspond to the surface area-integrated
 445 EKE (globally or over specific regions).

$$446 \langle \text{EKE} \rangle(t) = \iint_A \frac{1}{2}\rho_0(u'^2 + v'^2) dx dy, \quad (3)$$

447 where A refers to the area of each geographical or dynamical region, angle brackets $\langle \rangle$ denote the
 448 area integral, and $\langle \text{EKE} \rangle(t)$ has units of Jm^{-1} , as it is multiplied by the grid area.

449 Furthermore, the velocity field was decomposed into mesoscale (u_m, v_m ; scales smaller than
 450 3°) and large-scale (u_{ls}, v_{ls} ; scales larger than 3°). To decompose the velocity field, we first
 451 compute large-scale u_{ls} and v_{ls} by a spatial convolution with a constant $3^\circ \times 3^\circ$ kernel K :

$$452 \quad \vec{u}_{ls}(x, y, t) = \frac{\iint \vec{u}(x - x', y - y', t) K(x', y') dx' dy'}{\iint K(x', y') dx' dy'}, \quad (4)$$

453 the mesoscale \vec{u}_m is defined as:

$$454 \quad \vec{u}_m = \vec{u} - \vec{u}_{ls}. \quad (5)$$

455 Then the mesoscale and large-scale EKE can be computed using these velocity fields.

456 Sea surface temperature gradients

457 Analogous to mesoscale and large-scale EKE, sea surface temperature (SST) gradients are
 458 decomposed into mesoscale (SST gradients with scales smaller than 3°) and large-scale (SST gra-
 459 dients with scales larger than 3°). To decompose the SST gradients, we first compute large-scale
 460 SST by using a spatial convolution with a constant $3^\circ \times 3^\circ$ kernel K , and a 12-month running
 461 average i.e.,

$$462 \quad \text{SST}_{ls}(x, y, t) = \frac{\iint \widetilde{\text{SST}}(x - x', y - y', t) K(x', y') dx' dy'}{\iint K(x', y') dx' dy'}, \quad (6)$$

463 where the tilde $\widetilde{}$ denotes a 12-month running average. The mesoscale SST is then defined as

$$464 \quad \text{SST}_m = \text{SST} - \text{SST}_{ls}. \quad (7)$$

465 The gradients of the large-scale and mesoscale SST are computed afterwards. The SST

⁴⁶⁶ gradient magnitude is:

$$\text{467} \quad |\nabla \text{SST}| = \sqrt{\left(\frac{\partial \text{SST}}{\partial x}\right)^2 + \left(\frac{\partial \text{SST}}{\partial y}\right)^2}, \quad (8)$$

⁴⁶⁸ with analogous expressions for SST_m and SST_{ls} .

⁴⁶⁹ Computations of SST gradient time-series and time mean SST gradient trend maps are anal-
⁴⁷⁰ ogous to those of EKE, e.g. the area-integrated SST gradients:

$$\text{471} \quad \langle|\nabla \text{SST}|\rangle(t) = \iint_A |\nabla \text{SST}| \, dx \, dy, \quad (9)$$

⁴⁷² Trends, significance & uncertainties

⁴⁷³ Linear trends are calculated using a linear least-squares regression for spatially integrated
⁴⁷⁴ time-series. For trend maps the fields are first coarsened to a $1^\circ \times 1^\circ$ grid, and then the linear trends
⁴⁷⁵ are computed for each grid point. All the observed trends for EKE and SST gradients (time-series
⁴⁷⁶ and trend maps) are assessed using a Theil-Sen estimator, while the statistical significance uses a
⁴⁷⁷ modified Mann-Kendall test²⁶. This statistical test takes into account autocorrelations within the
⁴⁷⁸ time-series. Finally, the reported uncertainties in figures 4c,e and 5c,e correspond to the standard
⁴⁷⁹ error using the effective sample size from the Mann-Kendall test; that is, the standard deviation of
⁴⁸⁰ the time-series divided by the square root of the effective sample size.

⁴⁸¹ Geographical and dynamical regions

⁴⁸² Geographical regions consist of the following ocean basins (see Fig.4d): the Southern Ocean
⁴⁸³ (south of 35°S), the Indian Ocean, the Pacific Ocean and the Atlantic Ocean. These ocean basins
⁴⁸⁴ were defined to capture ocean processes at all scales. The ocean basin mask can be obtained from

485 the repository 10.5281/zenodo.3993824 that contains all the data used for this study (refer
486 to data availability; filename ocean_basins_and_dynamical_masks.nc).

487 Dynamical regions were defined from the climatological mean SSH and the mean KE (see
488 Fig.5d). We defined a mask for each dynamical region, then we extracted and masked each dy-
489 namical region in the following order, to avoid any overlap between regions:

- 490 1. the equatorial region is defined as the region between 9°S and 9°N,
- 491 2. the boundary currents and their extensions are defined as regions with mean KE above the
492 ~99-th percentile (2.8σ). Note that the Peruvian and Californian currents are weaker (below
493 the 99th percentile of mean KE) and, therefore, according to our definition, they do not
494 qualify as boundary currents.
- 495 3. the subtropical gyre masks depend on each ocean basin: the Pacific Ocean gyres correspond
496 to mean SSH above the 0.65 m contour; the Atlantic Ocean gyres correspond to mean SSH
497 above the 0.36 m contour; and the Indian Ocean gyres correspond to mean SSH above the
498 0.60 m contour. All these values were tuned to approximately capture the same extension as
499 the theoretical estimation of ocean gyres according to the Sverdrup balance, and
- 500 4. the Antarctic Circumpolar Current and its surrounding areas (ACC) is defined as all remain-
501 ing regions left between 35°S - 60°S.

502 The dynamical regional mask can be obtained from the repository containing all the data used for
503 this study (refer to data availability; filename ocean_basins_and_dynamical_masks.nc).

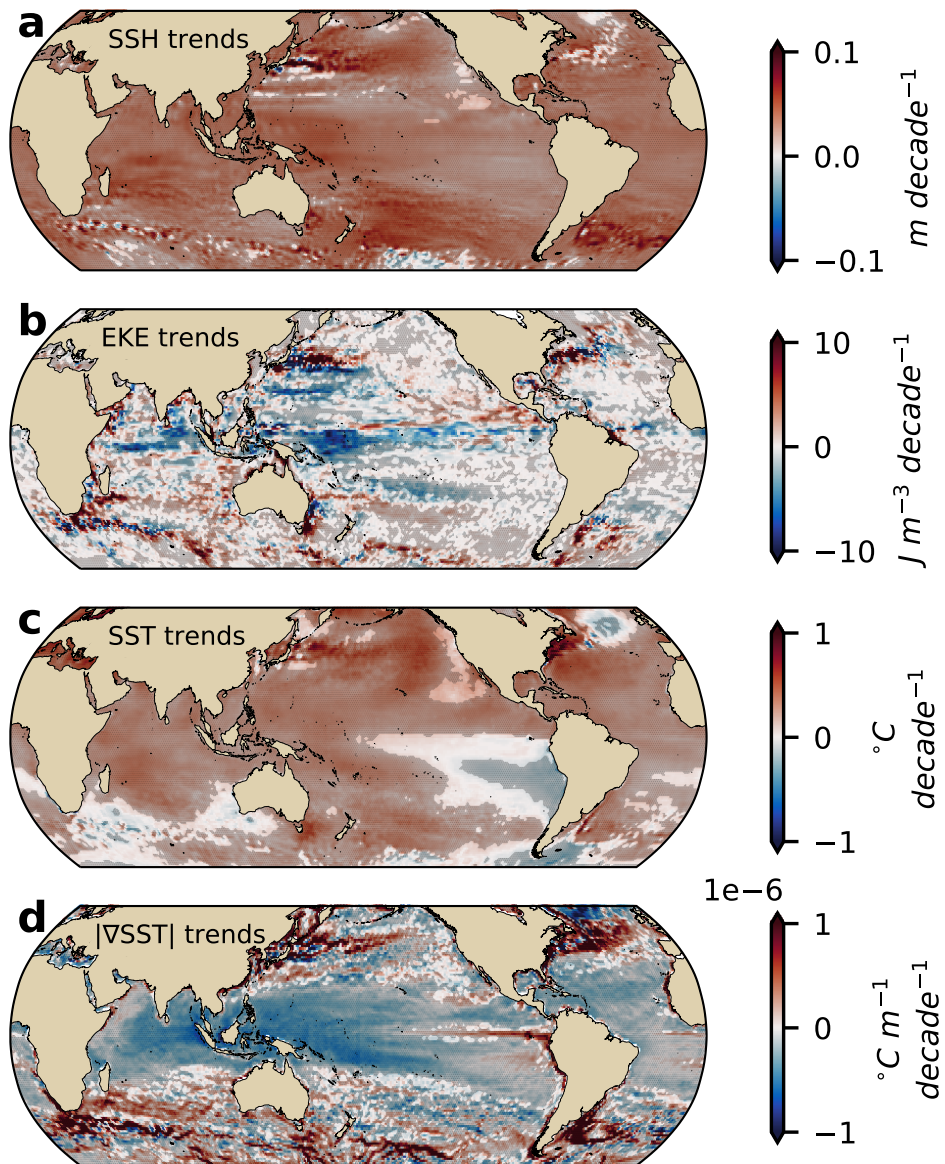
504 **Data availability**

505 The unprocessed data from the satellite altimetry (produced by Ssalto/Duacs and distributed
506 by AVISO+) can be found at: AVISO+ SSH products website). The processed data used in this
507 study is publicly available in netCDF format at 10.5281/zenodo.3993824.

508 **Code availability**

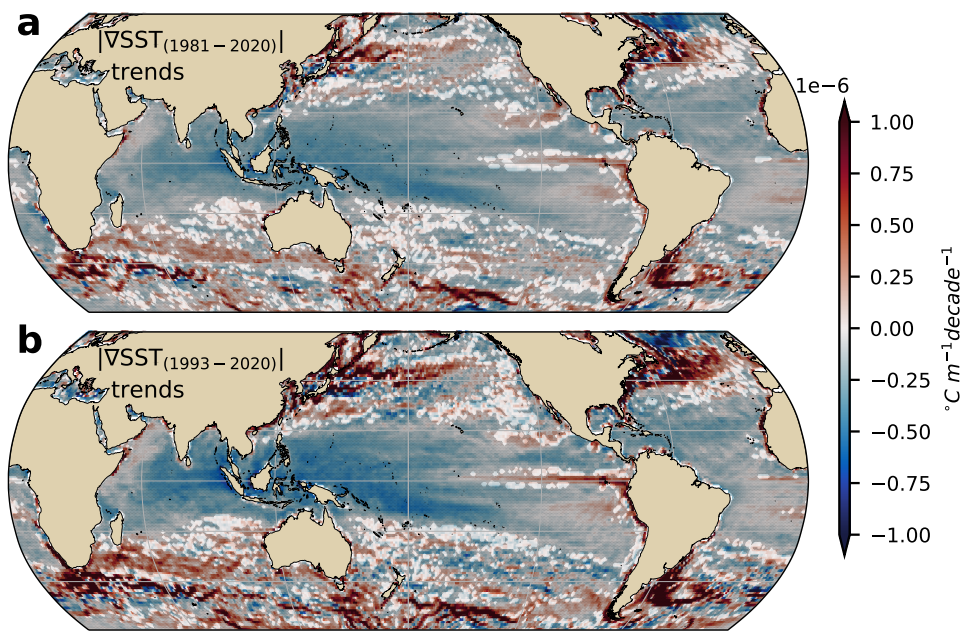
509 All plots were generated using Python 3.8. Additional information and notebooks that re-
510 produce the figures and analysis can be found at the xarrayMannKendall repository (10.5281/zen-
511 odo.4458777) and EKE_SST_trends repository (10.5281/zenodo.4458784).

512 **Extended data**

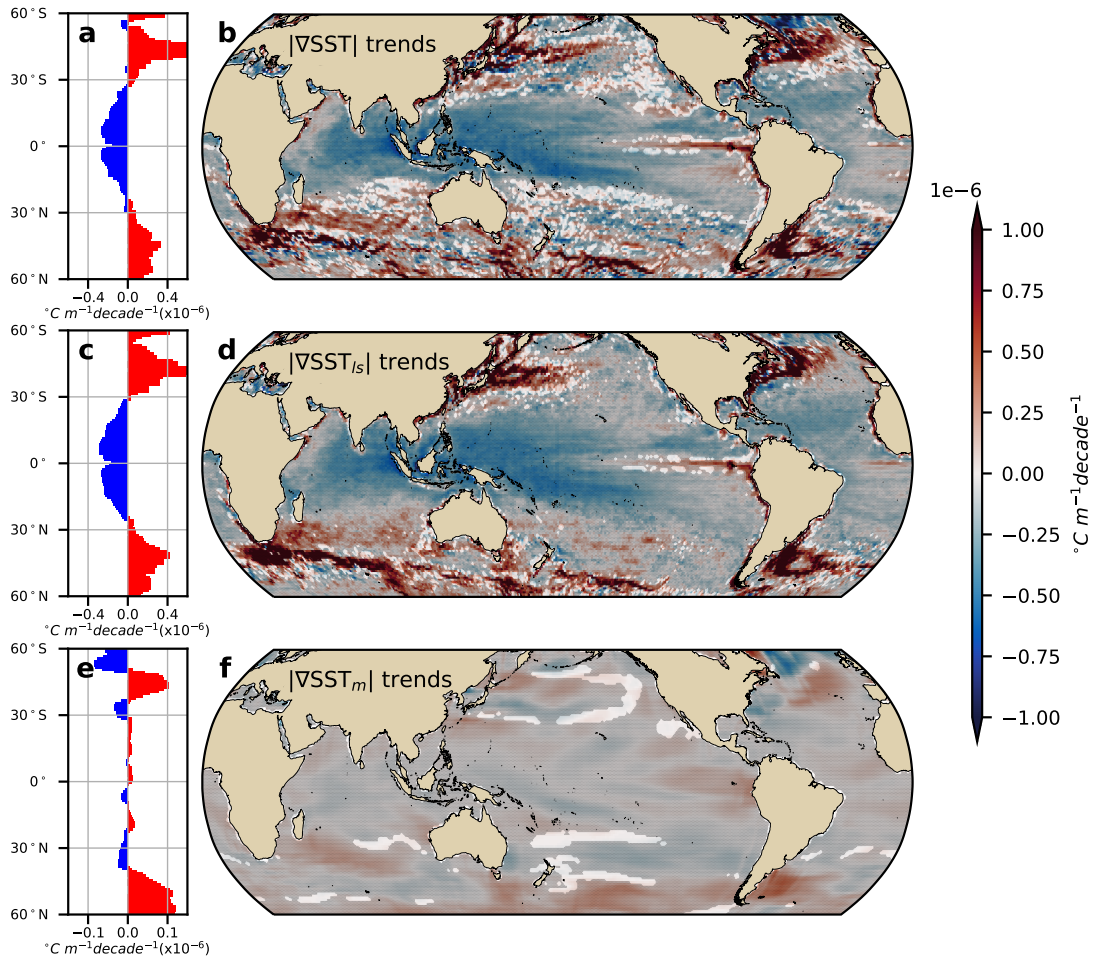


513

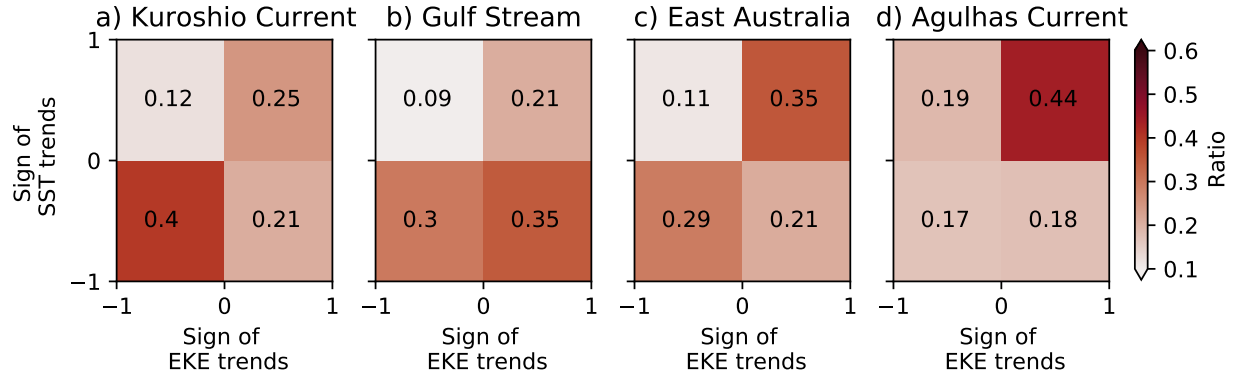
514 **Extended Data Figure 1 | Regions of statistically significant trends of (a) sea sur-**
515 **face height; (b) surface eddy kinetic energy; (c) sea surface temperature; (d) sea**
516 **surface temperature gradient magnitude.** As per Figs. 1b, 1f, 2b, and 2f in main
517 manuscript, but showing in gray stippling regions that are statistically significant above
518 the 95% confidence level.



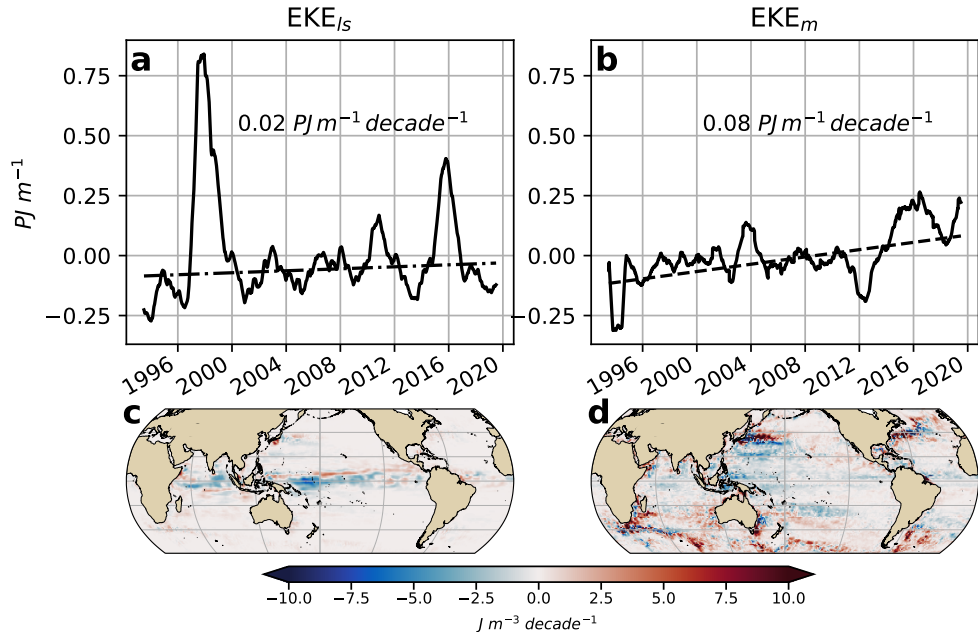
519
520 **Extended Data Figure 2 | Sea surface temperature gradient magnitude trends for**
521 **periods between 1981-2020 and 1993-2020.** Gray stippling shows regions that are sta-
522 tistically significant above the 95% confidence level.



523
 524 **Extended Data Figure 3 | Sea surface temperature gradient magnitude trend scale**
 525 **analysis.** Large-scale SST gradient magnitudes are computed by filtering the SST field
 526 with a 3° kernel filter and a running average of 12 months before computing the gradient
 527 magnitudes and their respective trends (see Methods). The small scales correspond to
 528 the gradients of the SST minus the large-scale filtered SST field. (a) Zonally averaged
 529 SST gradient magnitude trends; (b) map of SST gradient magnitude trends; (c) zonally
 530 averaged small-scale SST gradient magnitude trends; (d) map of small-scale SST gradi-
 531 ent magnitude trends; (e) zonally averaged large-scale SST gradient magnitude trends; (f)
 532 map of large-scale SST gradient magnitude trends. In panels (b), (d) and (f) gray stippling
 533 shows regions where the trends are statistically significant above the 95% confidence
 534 level.

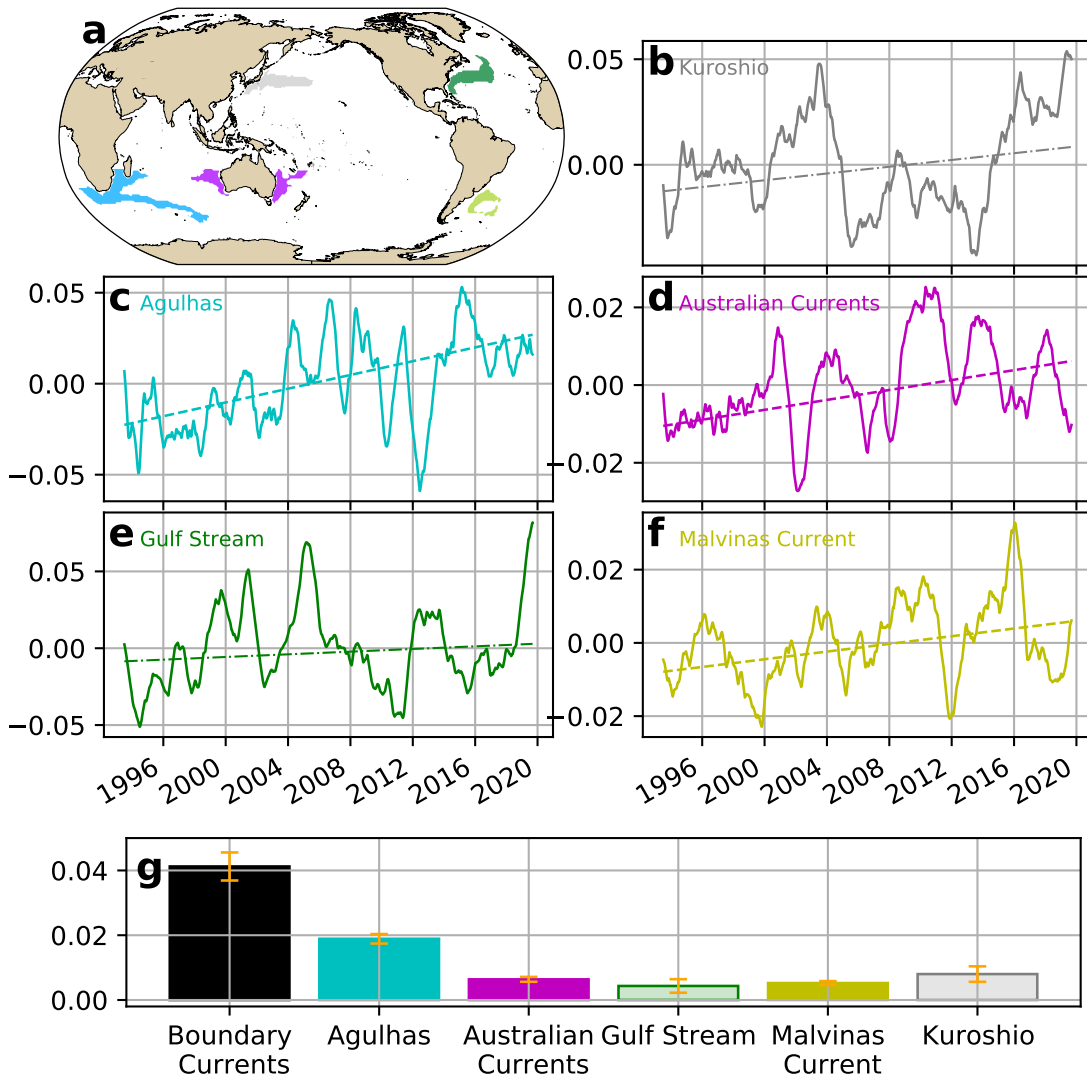


Extended Data Figure 4 | Regional ratio of mesoscale SST gradient magnitude trends and surface EKE trends signs. (a) Kuroshio current; (b) Gulf Stream; (c) East Australian Current; (d) Agulhas retroflection. The ratio was computed by integrating the area weighted sign of the SST gradient magnitude trends and surface EKE trends divided by the total area of the region plotted in the Fig. 3. Quadrants I and III of each panel show colocated regions with the same sign in SST gradients and EKE trends, more than 60% of the signs in the (a) Kuroshio current, (c) East Australian Current, and (d) Agulhas retroflection are colocated.

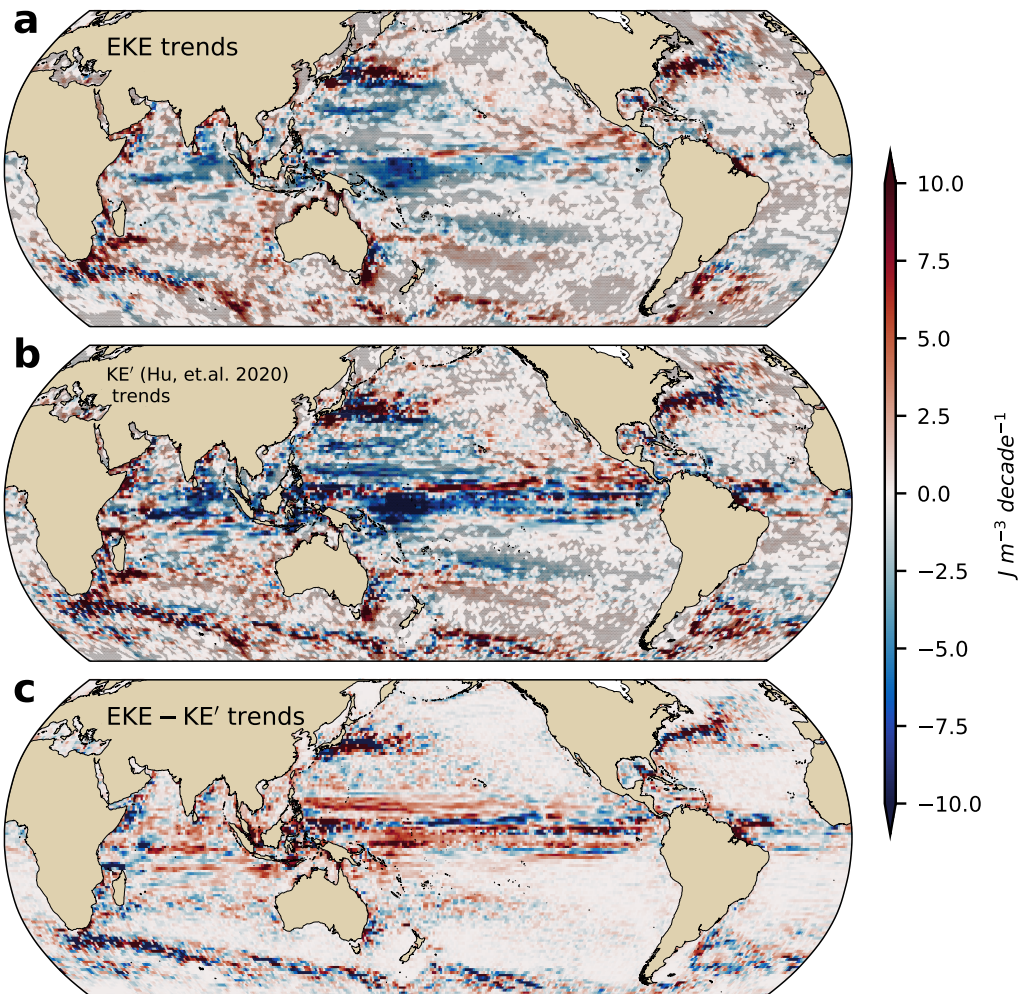


Extended Data Figure 5 | Surface eddy kinetic energy time-series and trends computed from filtered velocities. Scales larger than typical mesoscale are computed by filtering the surface velocity fields with a 3° kernel filter (u_{ls}), and the smaller scales are calculated from the difference of the velocity fields and the filtered velocity field ($u_e = u - u_{ls}$).

550 Then surface EKE and their respective trends are computed (see Methods). (a) EKE time
 551 series of scales larger than 3 degrees time series; (b) EKE time series of scales smaller
 552 than 3 degrees; (c) map of large-scale EKE trends; (d) map of small-scale EKE trends.
 553 Text in panels (a) and (b) correspond to trends per decade.



554
 555 **Extended Data Figure 6 | Time-series and trends of surface eddy kinetic energy in-**
 556 **tegrated over boundary currents.** (a) Map of boundary current regions defined from cli-
 557 matological mean EKE and time series anomalies ($PJ\ m^{-1}$) and trends ($PJ\ m^{-1}\ decade^{-1}$)
 558 for each boundary current : (b) Kuroshio Current; (c) Agulhas Current; (d) East Australian
 559 Current and Leewin Current; (e) Gulf Stream; (f) Malvinas Current. (g) Linear EKE trends
 560 for boundary currents, uncertainties are shown in orange bars and statistically significant
 561 trends (above the 95% confidence level) are denoted with solid bars while non-significant
 562 trends are translucent.



563
 564 **Extended Data Figure 7 | Comparison of satellite trends using surface EKE and ki-**
 565 **netic energy anomaly (KE') as computed by Hu et al., 2020¹⁵** (a) EKE trend map, (b)
 566 KE' trend map, and (c) difference between EKE and KE' trends. The difference between
 567 the fields is a consequence of the cross terms due to the Reynolds velocity decomposi-
 568 tion. In panel (a) and (b) gray stippling shows regions where the trends are statistically
 569 significant above the 95% confidence level.